AIAA SciTech Forum
13-17 January 2014, National Harbor, Maryland
32nd ASME Wind Energy Symposium

AIAA 2014-0710

The Effect of Various Actuator-Line Modeling Approaches on Turbine-Turbine Interactions and Wake-Turbulence Statistics in Atmospheric Boundary-Layer Flow

Pankaj K. Jha[1]
The Pennsylvania State University, University Park, PA, 16802

Matthew J. Churchfield[2] and Patrick J. Moriarty[3]
National Renewable Energy Laboratory, CO

Sven Schmitz[4]
The Pennsylvania State University, University Park, PA, 16802

When using an actuator-line representation of a wind turbine for computational fluid dynamics, it is common practice to volumetrically project the line force onto the flow field to create a body force in the fluid momentum equation. The objective of this study is to investigate how different volumetric projection techniques of the body force created by an actuator-line wind turbine rotor model affect the generated wake characteristics and blade loads in a turbine-turbine interaction problem. Two techniques for the body-force projection width are used, and they are based on either i) the grid spacing, or ii) the combination of grid spacing and an equivalent elliptic blade planform. An array of two NREL 5-MW turbines separated by seven rotor diameters is simulated within a large-eddy simulation solver subject to offshore neutral and moderately-convective atmospheric boundary-layer inflow. Power, thrust, and bending moment histories of both turbines, the statistics of angle of attack and blade loads over 2000 sec, variations in the mean and fluctuating velocity components, and turbulent kinetic energy and selected Reynolds stresses along vertical and spanwise sampling locations in the wake are analyzed. Comparisons for the different techniques of determining the body-force projection width of the actuator-line method are made and their effect on different physical quantities are assessed.

Nomenclature

ABL	=	Atmospheric boundary layer
ALM	=	Actuator line method
AOA	=	Angle of attack [degrees]
CFD	=	Computational fluid dynamics
D	=	Rotor diameter [m]
LES	=	Large-eddy simulation
MCBL	=	Moderately convective boundary layer
NBL	=	Neutral boundary layer
NREL	=	National Renewable Energy Laboratory
R	=	Blade radius [m]
RANS	=	Reynolds-Averaged Navier-Stokes
RPM	=	Revolutions per minute [1/min]
V_{wind}	=	Mean wind speed [m/s]

[1] Graduate Research Assistant, Department of Aerospace Engineering, AIAA Student Member
[2] Senior Engineer, National Wind Technology Center, AIAA Member
[3] Senior Engineer, National Wind Technology Center, AIAA Member
[4] Assistant Professor, Department of Aerospace Engineering, AIAA Member

I. Introduction

The wind industry faces a number of challenges today in developing wind farms both on shore and off shore. One such challenge involves wind turbine wakes that interact with turbines located downstream, with other wakes, and with the turbulent atmospheric boundary layer (ABL). The ABL has different stability states during a diurnal cycle, which strongly affect the structure and strength of the ABL's turbulence, thus affecting the array efficiency in a wind farm.[1,2] At this time, fully blade-resolved simulations subject to resolved turbulent inflow are only possible with hybrid Reynolds-averaged Navier-Stokes (RANS)-large-eddy simulation (LES). Such an effort using hybrid RANS-LES is currently being pursued at the Pennsylvania State University within the "Cyber Wind Facility" program.[3,4] These high-fidelity simulations represent the current state-of-the-art in high-performance computing of wind turbine rotors and can provide four-dimensional data akin to true experimental data campaigns. However, the associated computational cost is so exorbitant that only very small arrays of wind turbines, i.e. one or two wind turbine rotors, can be analyzed. This precludes the simulation of an entire wind plant. The actuator-line method (ALM), on the other hand, offers the potential for accurately predicting unsteady wind turbine wakes at a feasible computational cost. Recently, the ALM of Sørensen and Shen[5] has been implemented into an ABL-LES solver created with OpenFOAM.[6] by researchers at the National Renewable Energy Laboratory (NREL).[7-12] The solver has demonstrated its potential to model large wind farms and overall wake effects. Recent work by the authors eluded to some difficulties of the ALM in accurately predicting sectional blade loads, in particular at the blade tips. The authors developed a novel technique for determining a variable body-force projection width used within the ALM that gave improved predictions of the blade tip loads.[13,14] This was accomplished by having the body-force projection width being a function of an equivalent elliptic blade planform of the same aspect ratio as the original blade.

The focus of this work concerns finding answers to the important question of how the incorporation of a variable body-force projection width in the ALM, which improved the prediction of the blade loads, affects wake characteristics along with power, thrust, and bending moment histories of a turbine-turbine array. The array of large 5-MW turbines is submerged in ABL flow of various stability states. In this work, results are presented for two different techniques of determining the body-force projection width in the ALM with turbulent ABL inflow under two different stability states, neutral and moderately convective.

II. Numerical Methods

A. Atmospheric Boundary Layer Solver in OpenFOAM

The atmospheric boundary layer is simulated within a large-eddy simulation (LES) framework in OpenFOAM[6] that embeds the ALM. The governing equations and detailed information on the different terms in the continuity, momentum, and potential temperature equations are explained in earlier works.[7-9] For a stand-alone ABL precursor simulation, the term in the momentum equation that describes the body force associated with the actuator-line method is set to zero.

B. Actuator-Line Method (ALM) in OpenFOAM

The ALM is rooted in the work of Sørensen and Shen[5] and is being actively developed and maintained by researchers at NREL and Penn State.[7-14] The ALM finds sectional lift and drag forces by determining the local flow velocity and angle of attack (AOA) that is then applied to an airfoil lookup table. The blade is discretized into a finite number (typically 25-40) of actuator elements. The lift and drag forces computed at the center of these actuator elements are then projected onto the background Cartesian grid as body forces in the momentum equation. The last term in the momentum equation (1) corresponds to this body force,

$$\frac{D\boldsymbol{u}}{Dt} = \mathrm{RHS} + \mathbf{F}_p \tag{1}$$

The body-force term indirectly imposes pressure and velocity jump across the actuator line. The projection of the body forces that represent the blade loads is typically achieved by a Gaussian function as shown in equation (2),

$$\mathbf{F}_p\left(x_p, y_p, z_p, t\right) = -\sum_N \sum_m \mathbf{f}_{N,m}(x_{N,m}, y_{N,m}, z_{N,m}, t\ )\ \eta_{N,m} \tag{2}$$

where $$\eta_{N,m} = \frac{1}{\varepsilon^3 \pi^{3/2}} exp\left[-\left(\frac{|\boldsymbol{r}|}{\varepsilon}\right)^2\right] \ . \tag{3}$$

Here N is the blade index, m is the actuator point index, and $|\boldsymbol{r}|$ is the distance from the grid cell to the actuator point. Recent advances were made by the authors[13, 14] on varying the body force projection width, or Gaussian radius ε, such that an improved prediction of the spanwise blade loads was obtained. This was accomplished by using a variable Gaussian radius ε along the blade span that is determined using an equivalent elliptic planform c*. Details can be found in recent papers.[13,14] The following techniques for determining ε are used:

$$\textbf{Grid-based } \boldsymbol{\varepsilon} \qquad \boldsymbol{\varepsilon/\Delta r = const. = 2}$$

$$\textbf{Elliptic } \boldsymbol{\varepsilon} \qquad \boldsymbol{\varepsilon/c^{*} = f(r, \Delta r, AR)} \tag{4}$$

As mentioned above, the focus of this work is to answer the question of how these two techniques for determining the body force projection width, or Gaussian radius ε, affect the time-varying blade loads and wake-turbulence statistics.

C. Computational Methodology

A precursor ABL simulation is first performed on a grid of normal hexahedral cells that typically extends 3 km x 3 km x 1 km in the two horizontal directions and the vertical direction, respectively, with resolution of about 10 m. The simulation is run until a quasi-stationary state is achieved, which commonly takes between 10,000 s and 30,000 s, depending in large part upon the atmospheric stability simulated. The simulation is then continued for 2,000 s to extract precursor boundary-layer data at the inlet plane at some sampling frequency. These boundary data serve as inflow to the actual ALM simulations. Simulation statistics are collected and analyzed as the simulation progresses.

The ALM simulations, forced by precursor boundary-layer data, are performed on grids of type and resolution that the authors have found to give accurate and consistent results.[13,14] An illustration is given in Fig. 1. Typically, 3 to 4 layers of grid refinement are performed in the region surrounding the turbines and their wakes, starting with the original grid used for the ABL precursor simulation. The refinement is done by splitting cells in half in each direction within each successive refinement zone. A grid resolution of 2.5 m near the turbine is used as a baseline. This is the finest grid resolution of the innermost grid, and it is maintained up to the end of the region of interest to allow the proper resolution of the smaller scale important turbulent structures generated by the turbine blades and the turbine wakes. As mentioned in Section II.B, two different techniques are used to determine the body force projection width, or Gaussian radius ε.

Time-averaging of the AOA, blade loads, turbine power, bending moment, velocity components and selected Reynolds stresses at various locations in the wake of both turbines start after 100 seconds of real time when initial transients have subsided is performed. The time-averaging has been performed for several eddy-turnover times of the forcing ABL inflow.

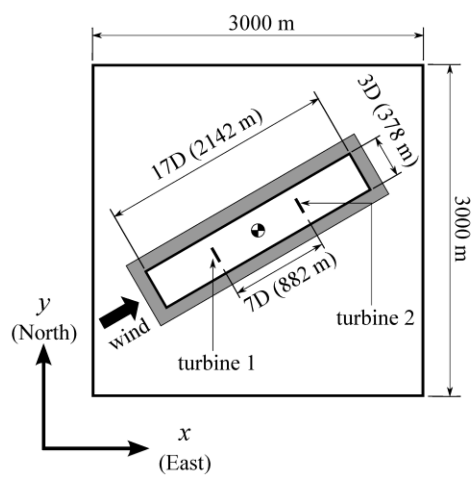

Figure 1. Computational domain used for turbine-turbine interaction problem.

III. Results and Discussion

A. Atmospheric Boundary Layer Simulations

The ABL simulations were performed for a neutral boundary layer (NBL) and moderately-convective boundary layer (MCBL) with a surface-temperature flux of 0.04 K-m/s. The surface roughness was chosen to be 0.001 m, which is typical for the ABL over sea. The wind speed at hub height (90 m) was forced to be 8 m/s. The grid used had dimensions: 3 km x 3 km x 1 km with a coarse resolution of 10 m followed by various layers of grid refinement, see Fig. 1. The simulation was performed until a quasi-stationary state was achieved. This time was found to be 18,000 s for NBL and 10,000 s for MCBL. Figure 2 shows mean velocity profiles and energy spectra of the ABL simulations. Precursor data to be used in the actuator line simulations were stored for the subsequent 2,000 s at an interval of 5 s. These precursor data serve as boundary condition at the inlet plane for subsequent ALM simulations using the aforementioned techniques to determine ε. Figure 2(a) shows the vertical variation of mean axial velocity for the two ABL states. The velocity gradient near the surface is larger for the NBL than for the MCBL and is expected to have substantial effect on the power production of the two turbines. Figure 2(b) shows the corresponding energy spectra. Figure 3 shows the turbulent structures for the two ABL states. In the MCBL case in Fig. 3(b), strong updrafts due to the temperature flux at the surface can be identified that do not occur in the NBL case in Fig. 3(a). Figure 4 shows the correlations of fluctuations in different velocity components and at different heights. It is apparent that the MCBL shows higher spanwise and vertical variances in Fig. 4b and 4c that are the cause of the enhanced turbulent mixing and transport phenomena compared to the NBL.

Both NBL and MCBL precursor data were used as ABL inflow to a turbine-turbine interaction problem consisting of two NREL 5-MW turbines[15] separated by 7 rotor diameters (D). The results are presented and discussed in the following sections.

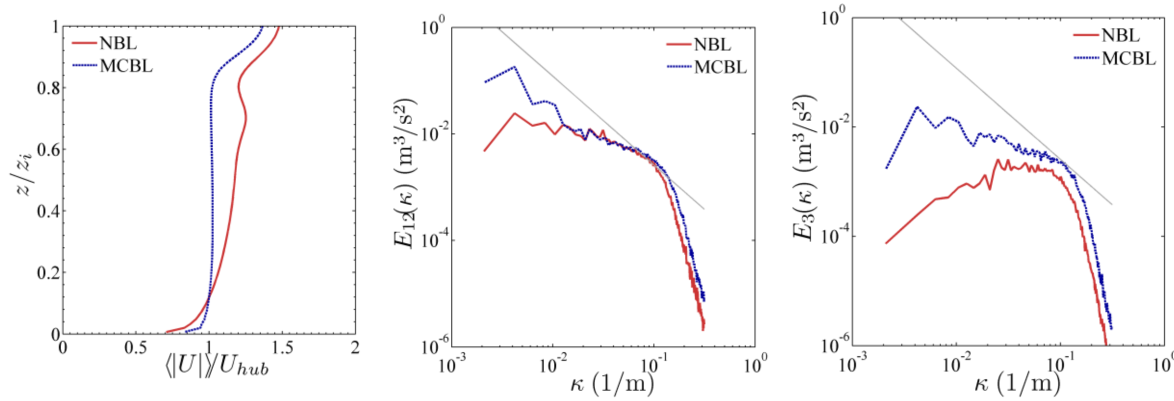

(a) **(b)**

Figure 2. Precursor ABL simulations.
NBL = Neutral boundary layer , MCBL = Moderately convective boundary layer
(a) Mean velocity profiles (b) Energy spectra

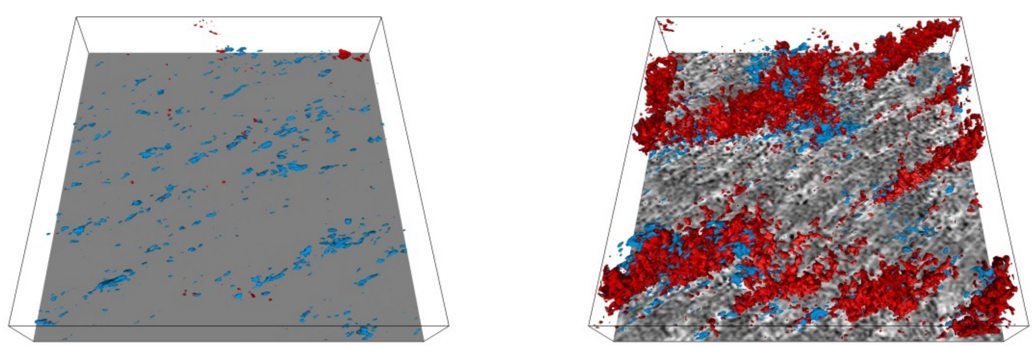

(a) NBL **(b) MCBL**

Figure 3. Iso-surface of instantaneous velocity fluctuations.

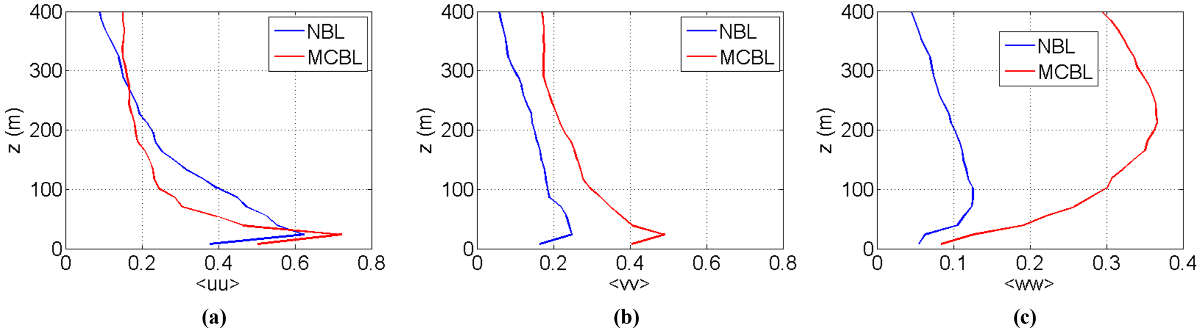

Figure 4. Velocity correlations of the ABL flow.

B. NREL 5-MW Turbines in NBL at V_{wind} (at hub) = 8 m/s

The simulations with the two turbines were performed for 2,000 s for which stored precursor data were available. The near-blade grid resolution was 2.5 m, and the time step of the ALM simulation was smaller compared to the precursor ABL simulations such that the actuator line tips do not traverse more than one grid cell per time step. This constraint is similar to a CFL criterion based on the rotor tip speed. The time-step size was chosen to be 0.02 s corresponding to an average azimuthal step of 0.9 degree. Stored precursor boundary data were used as inflow boundary conditions; the opposite boundaries were outflow boundaries. The precursor boundary-data frequency need not coincide with the ALM simulation time step; the boundary data are linearly interpolated in time if need be.

The results presented here cover 2,000 s of real-time simulation with NBL as well as MCBL precursor inflow. The averaging was done starting from 100 s through 2,000 s (the transients disappeared by about 100 s as evidenced by time histories). This averaging time is several times the large-eddy-turnover time, which was found to be approximately 50 s. Therefore, the selected time interval is expected to be adequate to yield meaningful turbulence statistics. The mean velocity at hub height from the ABL simulation was 8 m/s. In order to get a better idea about the wake and velocity profiles, velocities were sampled along both a vertical line and a horizontal line at hub height for the entire 2,000 s of simulation time, saving line data every 1 sec (or 5 time steps).

Figure 5 shows instantaneous flow fields. Iso-contours of the z-component of vorticity are shown for the two types of body-force projection methods dicussed earlier. It can be seen that the wakes for the two cases exhibit small differences. However, it is unclear from Fig. 5 how different the two ALM approaches are. It becomes, therefore, imperative to quantify several physical parameters. In the following, section parameters such as the AOA and lift coefficients, which form the building block of the ALM, will be discussed. Next, the integrated quantities, in particular power, thrust, and bending moment, will be discussed. The blade loads affect the tip vortices and vortex sheets emanating from the turbines. Therefore, the effect of the ALM projection method on selected wake parameters will also be discussed.

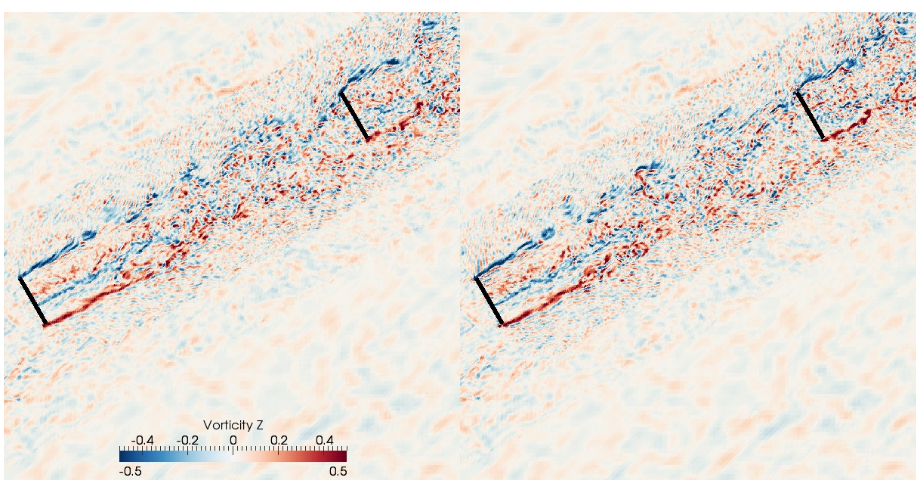

(a) $\varepsilon/\Delta_{grid}$ **(b) ε/c^***

Figure 5. Flow field in a horizontal plane through the hub.

B1. Sectional Blade Loads

The underlying method of any ALM starts with the determination of the flow-field velocity vector at the actuator points. These velocity components determine the local AOA at a given actuator point at each time step. Figure 6 shows spanwise distributions along the blades from both turbines of local mean and standard deviation (indicated as error bars) of section AOA for both ABL stability states. Results are shown for one blade at a time contrasting the two ALM spreading methods considered in this work. It can be observed in all the cases that a constant Gaussian spreading radius $\varepsilon/\Delta_{grid}$ leads to an over-prediction of AOA at the blade tips compared to those computed with the elliptic Gaussian radius ε/c^*. It should be noted that no tip correction was applied to the airfoil data. Both types of ALM spreading methods yield similar AOA distributions inboard of r/R = 0.85. In general, the inboard stations show higher mean as well as standard deviation. This can be attributed to the fact that the angular velocity component is smaller inboard compared to outboard along the blades. Therefore, it has less contribution to the local relative velocity. Hence an inboard local velocity vector is more sensitive to changes in the axial-inflow wind speed than their outboard counterparts. Furthermore, the mean AOA is higher inboard (r/R < 0.3) than it is outboard. Also, the standard deviations around the mean AOA at inboard stations are higher compared to outboard stations simply because of the higher sensitivity to changes in the axial rotor inflow. It can be seen that the local mean AOAs for turbine 1 in Fig. 6(a) and 6(c) are not that different for the two ABL stability states. In general, the mean AOAs are smaller for turbine 2 than for turbine 1 for both ABL conditions. This is, as will be shown later, because of the wake velocity deficit to which the second turbine is subject. The difference in AOA for turbine 2 in Fig. 6(b) and 6(d) is more pronounced for NBL than for MCBL because vertical turbulent mixing in the MCBL accelerates the recovery process of the wake velocity deficit. We can therefore conclude that the mean wind (or axial) component of the resultant velocity compared to the local angular velocity component is higher in the MCBL than in the NBL, thus resulting in turbine 2 having a higher mean AOA in MCBL flow than in NBL flow. The standard deviations in AOAs are in general larger for turbine 2 than for turbine 1 and for both ABL states because turbine 2 encounters turbulence due to both the ABL as well as the wake of turbine 1.

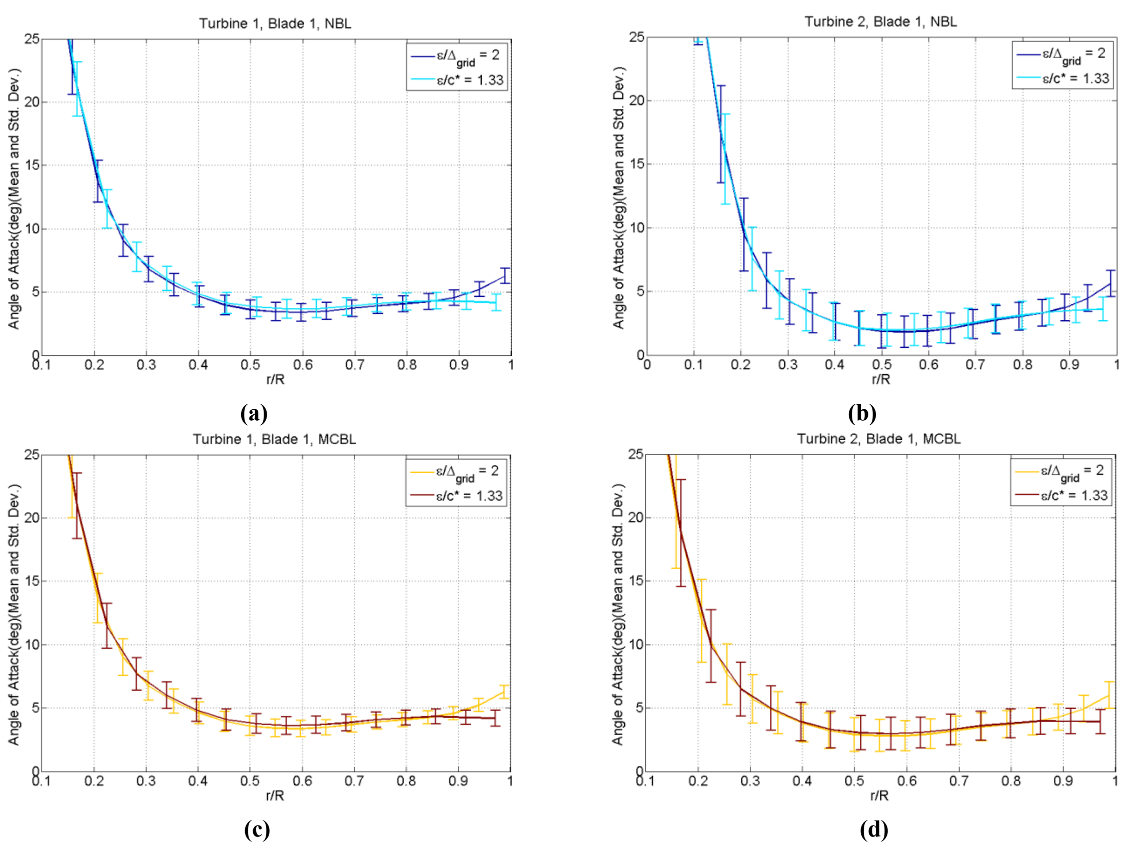

Figure 6. Mean and standard deviation of blade angle of attack (AOA).

(a) Turbine 1 (NBL) (b) Turbine 2 (NBL) (c) Turbine 1 (MCBL) (d) Turbine 2 (MCBL)

The discussion above pertains to the entire time interval under consideration. One question, though, that arises is how likely the local AOA was to be within a certain range. This can only be studied by looking at the probability density function (PDF) of the local AOA. Figure 7 shows the PDFs of the AOA for the two turbines and at the spanwise locations r/R = 0.340 and r/R = 0.914 that represent one inboard and one outboard station each. Comparisons are performed for the two types of ALM spreading for the Gaussian radius ε and the two ABL states. For both turbines and both ABL stability states, constant $\varepsilon/\Delta_{grid}$ spreading moves the PDF curve to a higher mean AOA at the outboard location r/R=0.914, which reflects the over-prediction of AOA observed in Fig. 6. The ALM spreading method does not shift the curves at the inboard location *r/R* = 0.340. Smaller AOAs for turbine 2 are again observed. Both inboard and outboard, the ABL state does not cause a shift in the curve for turbine 1. However, this is different for turbine 2 where the PDFs are shifted to higher mean AOA for MCBL inflow, i.e., the AOAs for turbine 2 are higher in a MCBL than in a NBL at both inboard and outboard locations. This is consistent with the observations in Fig. 6. Moreover, the PDF curves for turbine 2 are in general flatter than the corresponding curves for turbine 1, reflecting higher standard deviation. Also, the PDF curves for turbine 2 are not as smooth due to enhanced turbulence at the second turbine.

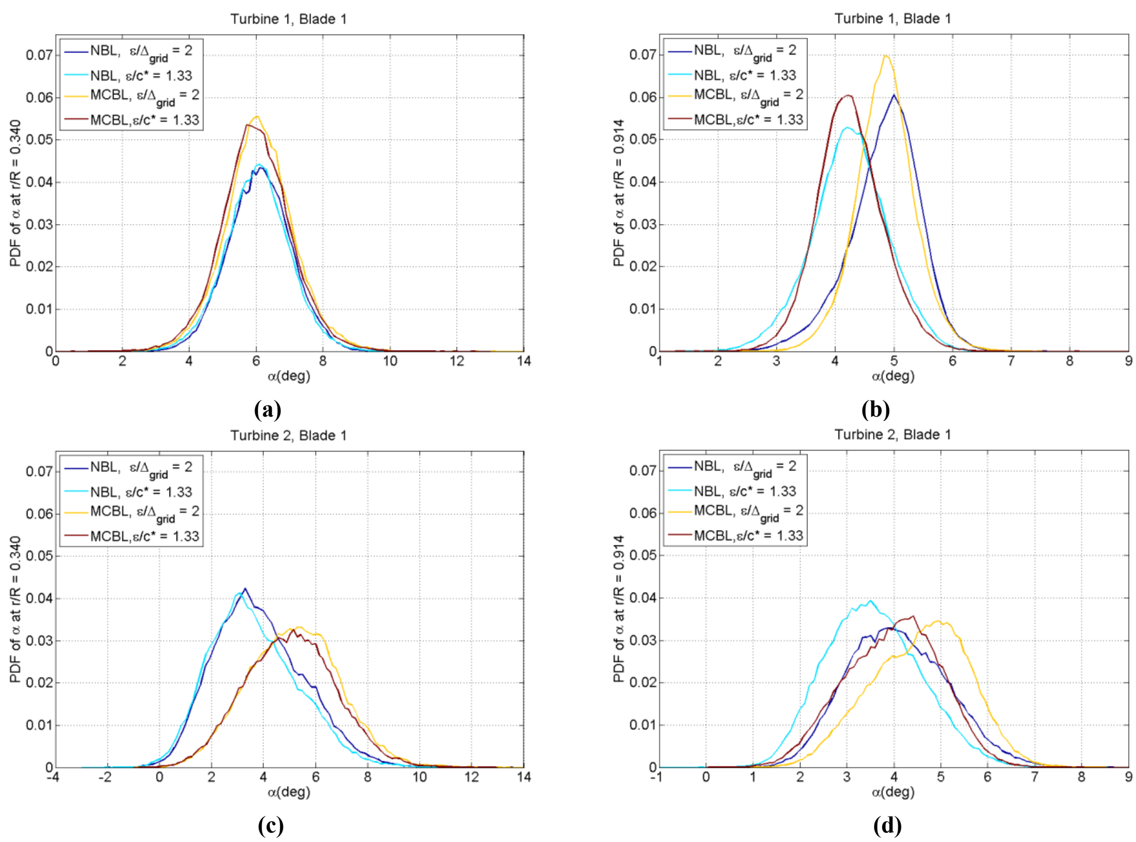

Figure 7. Probability density function (PDF) of blade angle of attack (AOA).
(a) Turbine 1, r/R = 0.34 (b) Turbine 1, r/R = 0.91 (c) Turbine 2, r/R = 0.34 (d) Turbine 2, r/R = 0.91

Figure 8 shows power spectral density (PSD) of computed AOAs for turbine 1 and spanwise locations r/R = 0.340 and r/R = 0.914 for both NBL and MCBL inflow. The sampling frequency was 50 Hz corresponding to the simulation time step of 0.02 s. Comparisons are again made for the two types of ALM spreading methods. Figure 9 shows the corresponding plots for turbine 2. For both turbines and both NBL and MCBL inflow conditions and for each of the spreading methods, the dominant frequency inboard is the rotational frequency 1/rev, i.e., about 0.15 Hz (or 9 RPM). The higher harmonics of *n*(1/rev)* are also visible in Figs. 8-9 and more pronounced at the outboard station r/R = 0.91. This is most likely due to the fact that the tip loads are more sensitive to the ABL turbulence. For each turbine, inboard as well as outboard, the NBL and MCBL stability states do not seem to make any noticeable difference to the PSD. However, for each turbine and for each stability state, the spreading method affects the spectra at the outboard station r/R = 0.91. Compared to turbine 1, the PSD for turbine 2 is higher at lower frequencies for both the NBL and MCBL states inboard as well as outboard. The ALM spreading method appears to affect the power spectra predominantly at the outboard station. The ALM method using an elliptic distribution of the Gaussian radius with ε/c^* reduces the fluctuations in the PSD corresponding to the highest frequencies. This means that the ALM method using ε/c^* is more sensitive to the higher frequencies (or smaller-scale turbulence) than the one using a constant Gaussian radius defined by $\varepsilon/\Delta_{grid}$. It is interesting to note that the ALM spreading methods do not affect the PSD at the inboard station r/R = 0.340. This observation is in agreement with those made for the AOA variation along the blade span where tip loads (r/R > 0.85) are quite different between the two ALM methods.

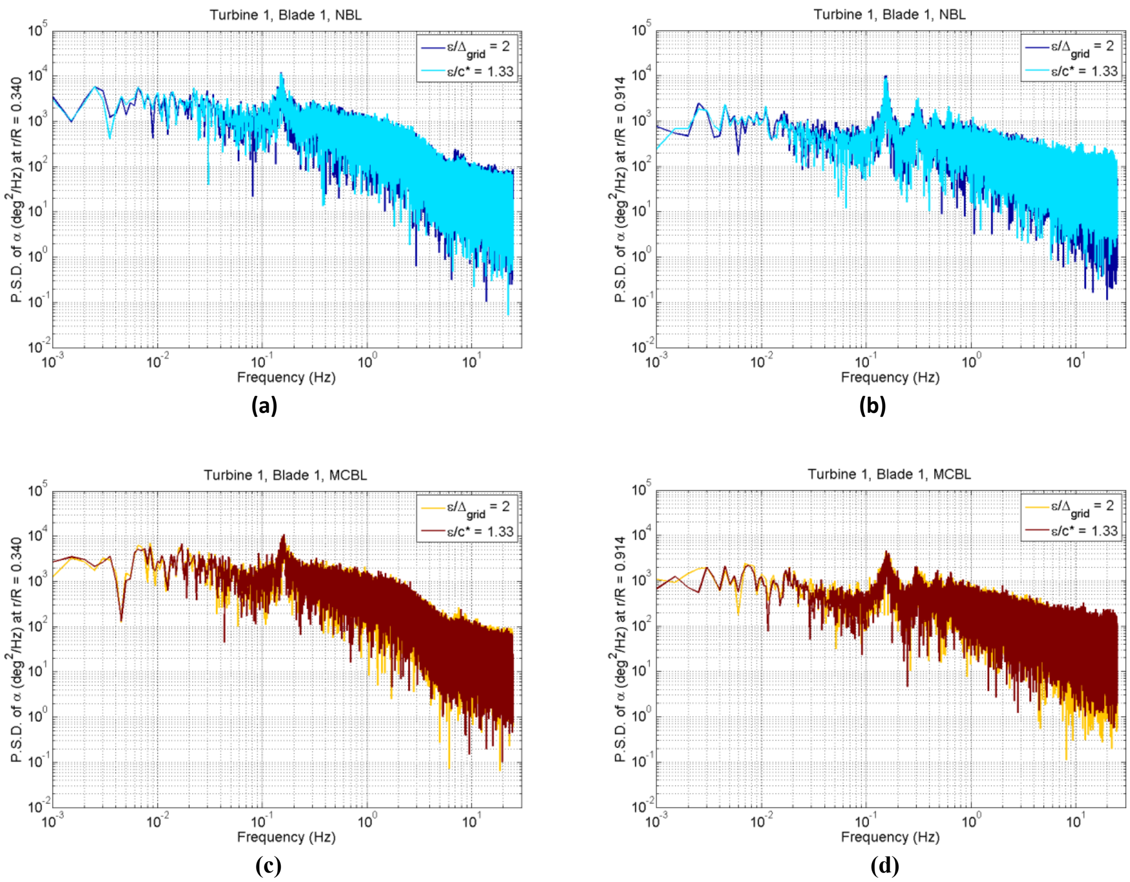

Figure 8. Power spectral density (PSD) of angle of attack (AOA) at selected spanwise stations.

(a) Turbine 1, r/R = 0.34 (NBL) (b) Turbine 1, r/R = 0.91 (NBL)
(c) Turbine 1, r/R = 0.34 (MCBL) (d) Turbine 1, r/R = 0.91 (MCBL)

Once the AOAs are determined locally at the actuator points, the next step in the ALM is to look up the aerodynamic force coefficients from the airfoil data tables and to compute local blade forces. Figure 10 shows the mean and standard deviation as error bars in local sectional lift coefficient for one selected blade of the two turbines and for the two ABL states, i.e. NBL and MCBL. Again, comparisons are made for the two types of spreading methods. The observations here are in line with those for the local AOAs in Fig. 6, as expected. It is apparent that turbine 1 operates at overall higher AOAs compared to turbine 2. However, the standard deviation in the sectional lift coefficient is significantly higher along the blade span of turbine 2 than it is for turbine 1. Furthermore, it can be seen that the most inboard stations operate at high lift coefficients. It is therefore reasonable to assume that inboard blade stations operate under unsteady aerodynamic conditions including separation and dynamic stall, both of which are currently not included in the simulations.

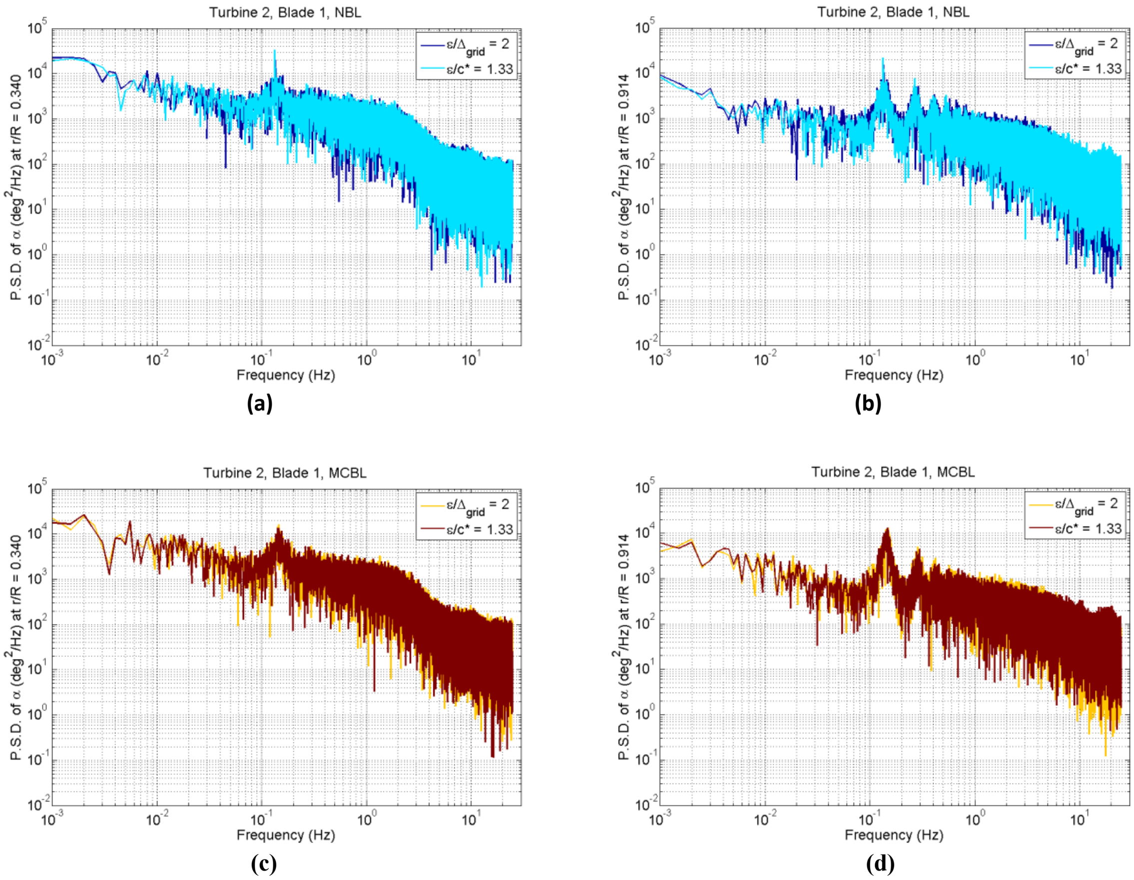

Figure 9. Power spectral density (PSD) of angle of attack (AOA) at selected spanwise stations.
(a) Turbine 2, r/R = 0.34 (NBL) (b) Turbine 2, r/R = 0.91 (NBL)
(c) Turbine 2, r/R = 0.34 (MCBL) (d) Turbine 2, r/R = 0.91 (MCBL)

B2. Integrated Quantities

The sectional blade loads when integrated along the span yield power, thrust, and root-flap bending moment. Figure 11 shows the power histories of the two turbines for the two ABL states. In each subfigure, comparisons are made between the two ALM spreading methods. For both turbines, the power for the second turbine is lower than the first turbine due to a velocity deficit in the wake that has not fully recovered at turbine 2 (see also discussion on wake parameters). However, this power drop for the downstream turbine (turbine 2) is more pronounced for the NBL than for the MCBL. This is attributed to the fact that for the MCBL, higher turbulent mixing relative to the NBL helps to recover the wake velocity deficit at a higher rate. Higher fluctuations in the power for both the turbines are visible for MCBL flow, which is again associated with higher turbulence levels due to enhanced mixing as a result of surface heating. The effect of the ALM spreading method can also be observed. For each turbine and for each ABL state, constant Gaussian spreading according to an $\varepsilon/\Delta_{grid}$ criterion leads to higher peaks, which is attributed to the over-prediction of blade tip loads as seen in Figs. 6 and 10. The time trace of integrated power clearly shows a range of frequencies. The lower frequencies can be attributed to the average eddy turnover time in the respective ABL flows, which are of higher amplitude in the MCBL flow compared to the NBL flow and attributed to higher vertical velocity fluctuations in the MCBL compared to the NBL (see Fig. 3).

More insight about the frequencies can be gained from the spectra of integrated power. Figure 12 shows the PSD of the two turbines for the two ABL states and with comparisons made between the two ALM spreading methods. Since the integrated power incorporates the accumulated effects of all three blades, the dominant frequency here is *3/rev*. It is apparent from Fig. 12 that the incoming mean wind shear is indeed responsible for the dominant PSD peak reflected at *3/rev* (or *0.45 Hz*). The higher harmonics of *n*(3/rev)* can also be seen in Fig. 12 and occur because of the fluctuating velocity components that result in a different incoming mean shear flow for every single blade revolution. These higher harmonics have most contributions from the outboard spanwise blade locations as observed in the spectra of AOAs in Figs. 8 and 9. The effect of the elliptic ALM spreading method according to a ε/c^*

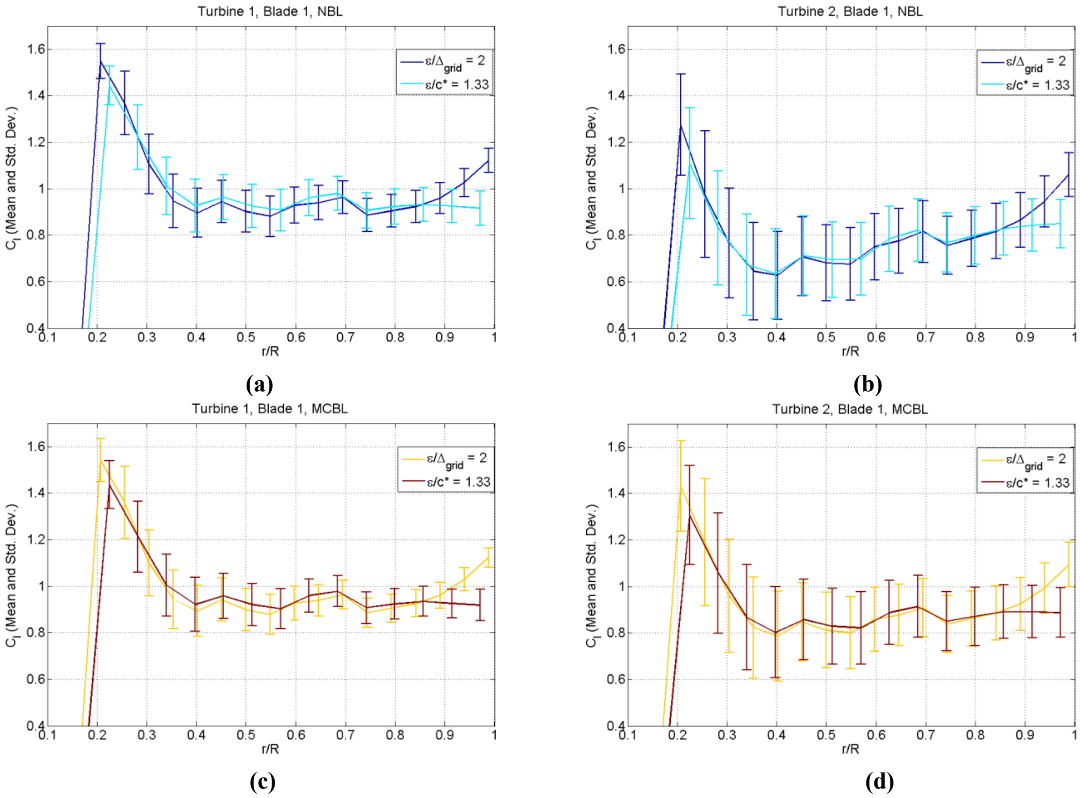

Figure 10. Mean and standard deviation of local coefficient of lift (c_l).
(a) Turbine 1 (NBL) (b) Turbine 2 (NBL) (c) Turbine 1 (MCBL) (d) Turbine 2 (MCBL)

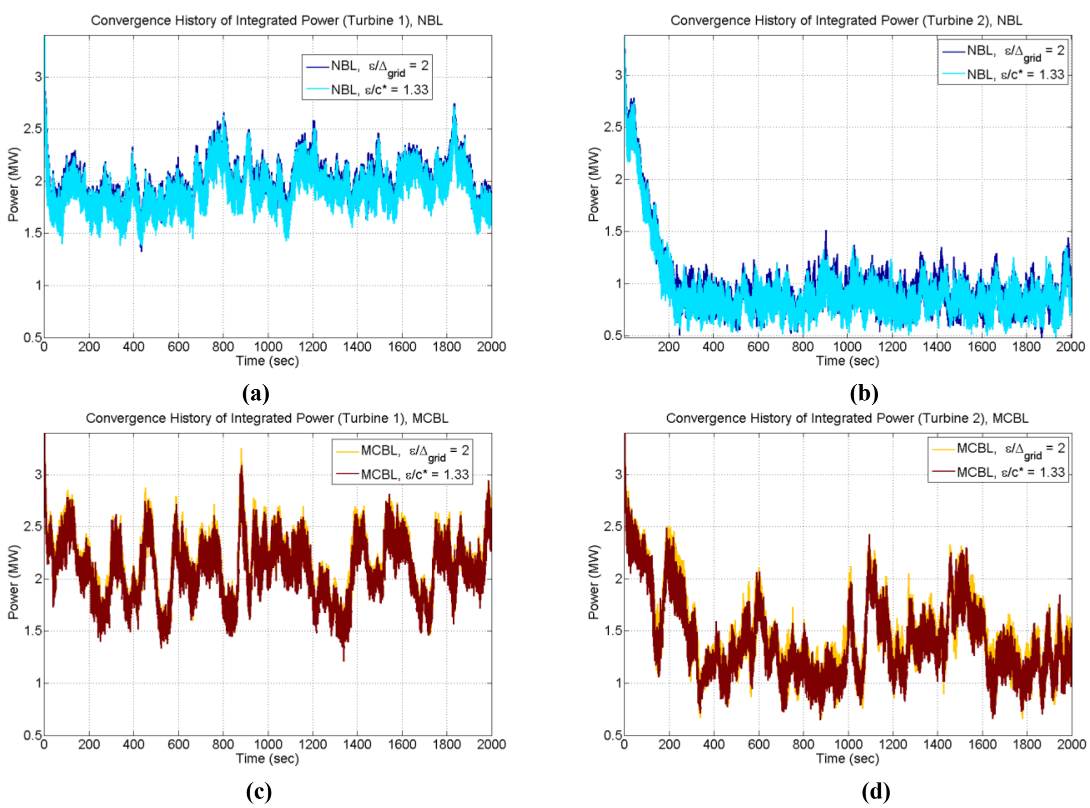

Figure 11. Power histories for turbine-turbine interaction problem.
(a) Turbine 1 (NBL) (b) Turbine 2 (NBL) (c) Turbine 1 (MCBL) (d) Turbine 2 (MCBL)

criterion can be observed for the higher frequencies where the reduced tip loads compared to ALM spreading according to $\varepsilon/\Delta_{grid}$ in Fig. 10 lead to reduced fluctuations (or band width) in the PSD in Fig. 12.

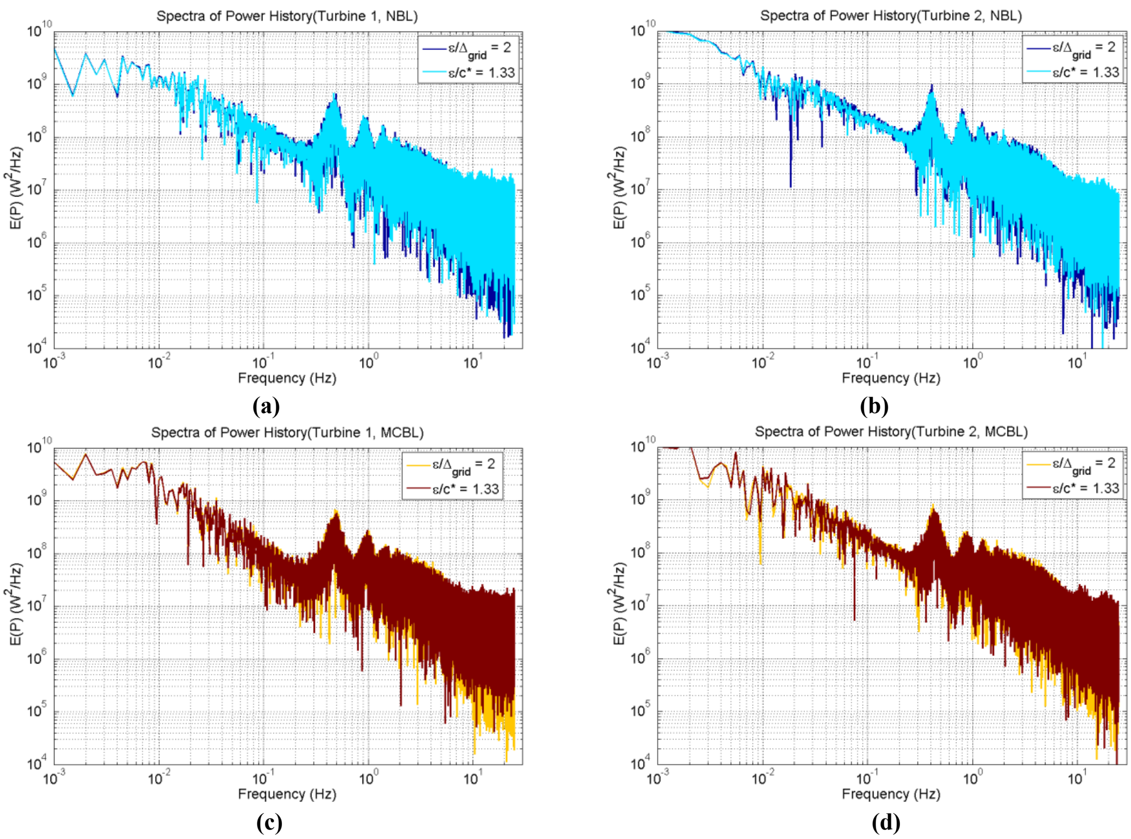

Figure 12. Power spectral density (PSD) of turbine power.
(a) Turbine 1 (NBL) (b) Turbine 2 (NBL) (c) Turbine 1 (MCBL) (d) Turbine 2 (MCBL)

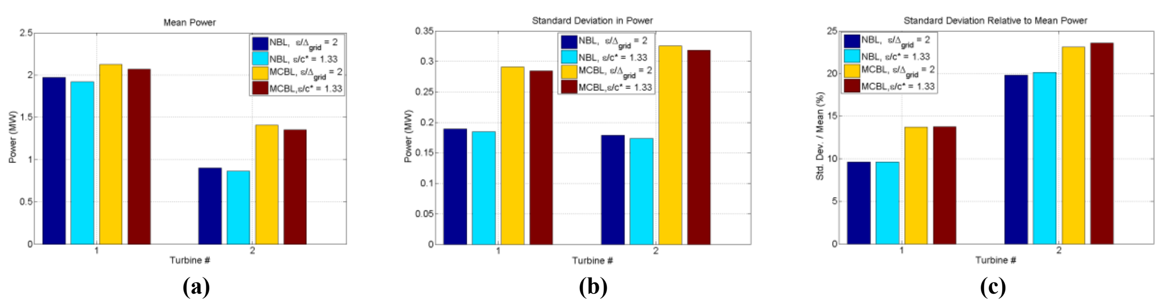

Figure 13. Mean and standard deviation of turbine power.
(a) Mean turbine power. (b) Standard deviation in turbine power.
(c) Standard deviation relative to mean turbine power

Figure 13 shows the mean, standard deviation, and the ratio of the two for the integrated power. Comparisons are made for the two ABL states, i.e. NBL and MCBL, and the two spreading methods. The observations for the mean and standard deviations for the two turbines are in accordance with their respective time traces, i.e., the mean power for turbine 2 is smaller than that of turbine 1. This is more pronounced in NBL flow as the wake does not recover as quickly in the absence of enhanced vertical mixing due to surface heating. For turbine 1, the ABL stability state does not have as much of an effect as does waking on turbine 2. The standard deviation in power for both turbines is higher in MCBL flow compared to NBL flow. The absolute values of standard deviation for turbine 2 compared to turbine 1 may be misleading. It is therefore more instructive to look at standard deviation normalized by the corresponding mean power. For both ABL states, the ratio of standard deviation to mean power is almost twice as much for turbine 2 compared to turbine 1. With regards to the effect of the ALM spreading method, both the mean power and the standard deviation are affected for both turbines and both ABL states. In general, elliptic spreading leads to lower predicted values due to reduced tip loads. The numerical values are given in Tables 1 and 2, respectively. The difference in mean power due to the ALM spreading method is about 2.6 – 2.7 % for turbine 1 and about 4 -4.2 % for turbine 2. A difference of 4% is not insignificant for an array of wind turbines since it may result in an over-estimation of array efficiency. It is not surprising that turbine 2 exhibits an accumulated effect of differences in the ALM spreading methods as discrepancies in wake parameters downstream of turbine 1 are amplified through an additional ALM step at turbine 2. It is anticipated that the difference due to spreading would be further augmented if more turbines are placed downstream because of the accruing difference as mentioned above. Further simulations with more turbines may shed some light on this behavior, which is beyond the scope of the current work.

Table 1: Mean power for the turbines.

Mean Power (MW)		**Turbine 1**	**Turbine 2**
NBL	Constant ε	1.9732	0.9023
	Elliptic ε	1.9217	0.8644
	% Difference	***2.61***	***4.20***
MCBL	Constant ε	2.1249	1.4072
	Elliptic ε	2.0671	1.3512
	% Difference	***2.72***	***3.98***

Table 2: Standard deviation in power for the turbines.

Std. Dev. in Power (MW)		**Turbine 1**	**Turbine 2**
NBL	Constant ε	0.1894	0.1787
	Elliptic ε	0.1848	0.1739
	% Difference	***2.43***	***2.69***
MCBL	Constant ε	0.2911	0.3255
	Elliptic ε	0.2848	0.3187
	% Difference	***2.16***	***2.09***

Figure 14 shows the time trace, Fig. 15 shows the spectra, and Fig. 16 shows the statistics of integrated bending moment for one selected blade of each turbine and for the two ABL stability states. Comparisons are again made for the two ALM spreading methods. The observations here are similar to those for the power barring a few subtle differences. First, the dominant frequency in each case is the rotational frequency *1/rev* due to the fact that only one blade is considered in the analysis. The difference due to the ALM spreading method is less pronounced compared to that for power as evidenced by the numerical values for the bar diagrams in Tables 3 and 4. This may seem surprising at first sight but it is simply due to the fact that bending moment scales with the square of the mean wind speed, while power scales with the cube of the mean wind speed. Therefore, the observed discrepancies between both ALM spreading methods are most pronounced for the turbine power. Figure 17 shows the corresponding histories of the integrated rotor thrust for both turbines. Overall, the thrust histories in Fig. 17 show a similar pattern when compared to the bending-moment histories in Fig. 14, though with smaller differences. This can be attributed to the observed overprediction of blade tip loads for $\varepsilon/\Delta_{grid}$ ALM spreading in Fig. 10 that does indeed contribute to differences in rotor thrust. However, these differences are amplified in the bending moment due to the large lever arm of the outboard stations compared to the inner portions of the blades.

B3. Wake Parameters

So far, we have looked exclusively at the loads and integrated quantities for the two turbines. We have discussed the differences in the sectional loads, integrated quantities, and the relation between them. It is equally important, however, to gain a deeper understanding of how the turbine wakes develop under different ABL stability states and what impact the ALM spreading methods have on the wake and how the differences between them affect the performance of the downstream turbine. We proceed by analyzing mean velocity profiles and other turbulence statistics along horizontal lines at hub height and along vertical lines at different downstream locations.

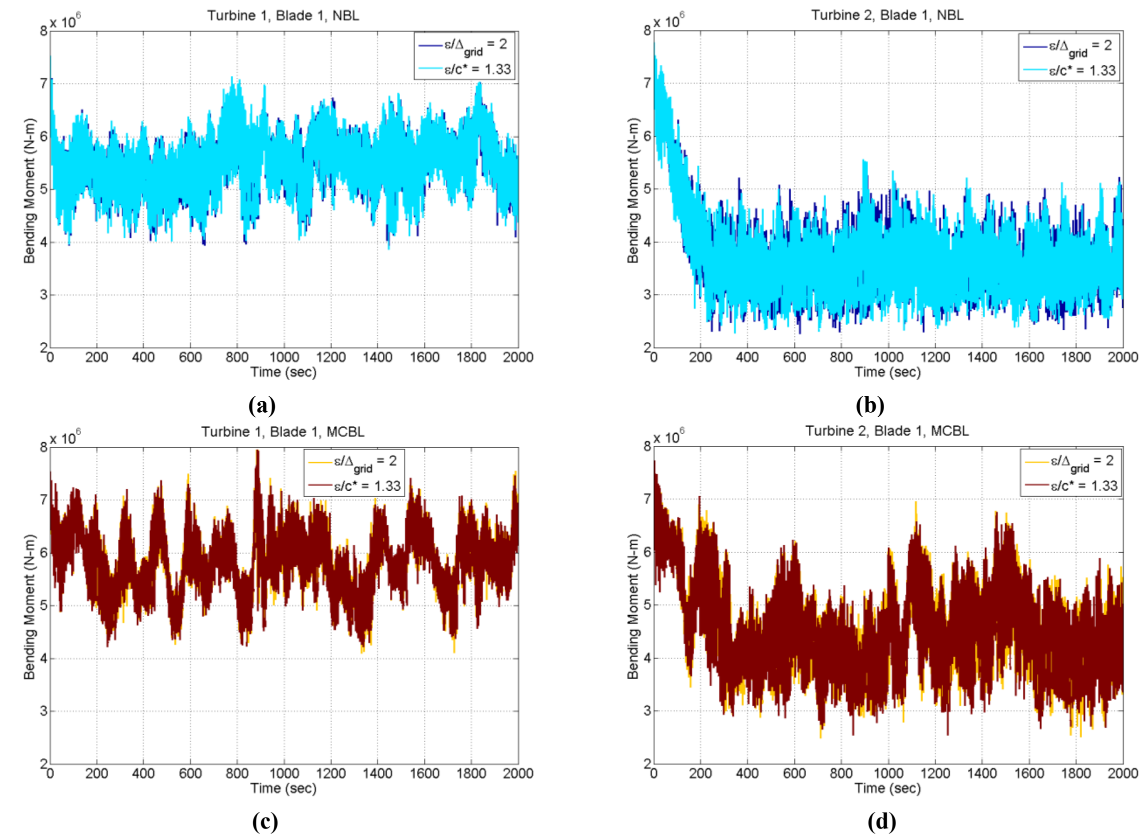

Figure 14. Blade bending moment histories for turbine-turbine interaction problem.
(a) Turbine 1 (NBL) (b) Turbine 2 (NBL) (c) Turbine 1 (MCBL) (d) Turbine 2 (MCBL)

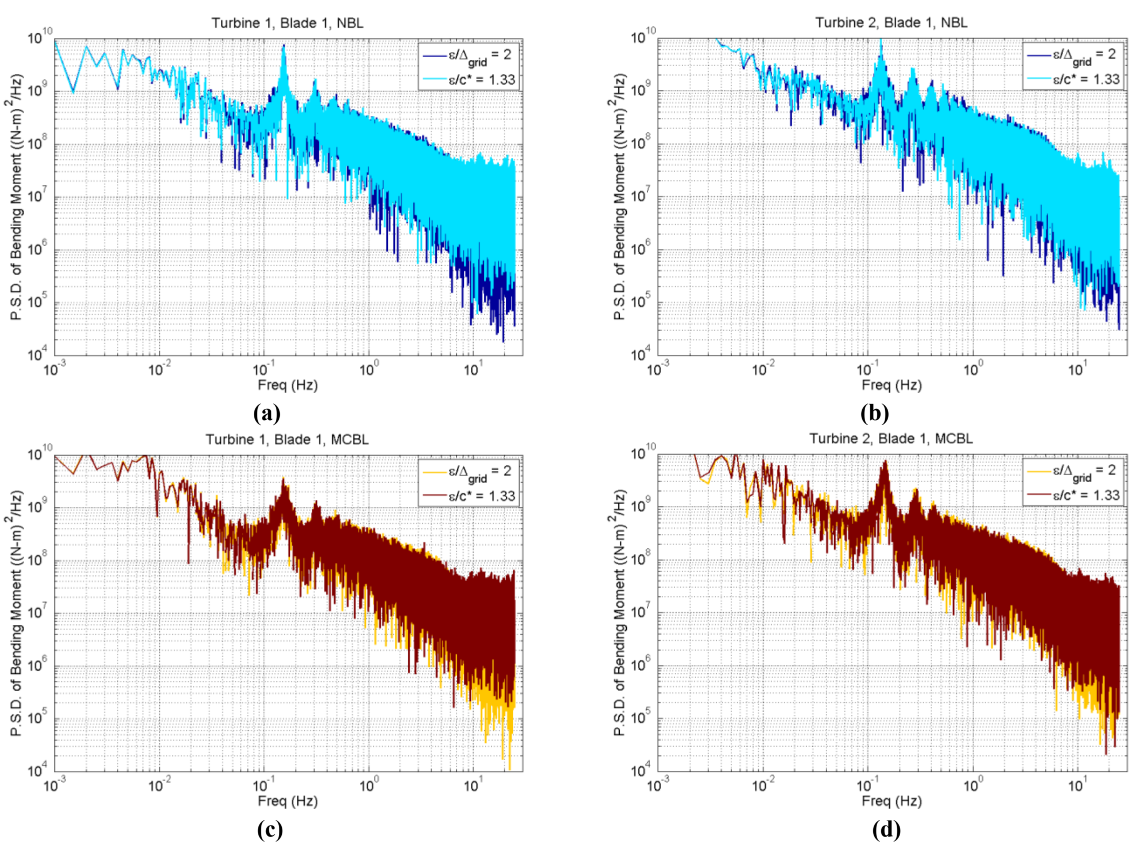

Figure 15. Power spectral density (PSD) of blade bending moment.
(a) Turbine 1 (NBL) (b) Turbine 2 (NBL) (c) Turbine 1 (MCBL) (d) Turbine 2 (MCBL)

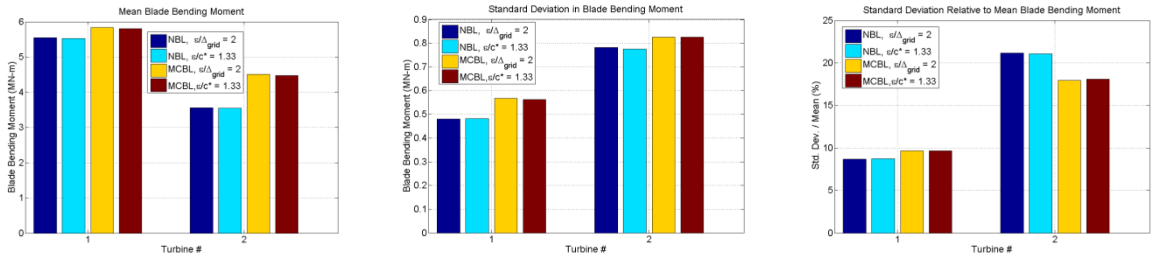

(a) (b) (c)

Figure 16. Mean and standard deviation in bending moment.
(a) Mean blade bending moment. (b) Standard deviation in blade bending moment.
(c) Standard deviation relative to mean blade bending moment

Table 3: Mean bending moment for one turbine blade.

Mean BM (x10^6 Nm)		**Turbine 1**	**Turbine 2**
NBL	Constant ε	5.5441	3.5621
	Elliptic ε	5.5285	3.5497
	% Difference	***0.28***	***0.35***
MCBL	Constant ε	5.8324	4.5134
	Elliptic ε	5.8076	4.4754
	% Difference	***0.43***	***0.84***

Table 4: Standard deviation in root-flap bending moment for one turbine blade.

Std. Dev. in BM (x10^6 Nm)		**Turbine 1**	**Turbine 2**
NBL	Constant ε	0.4746	0.5190
	Elliptic ε	0.4750	0.5124
	% Difference	***-0.08***	***1.27***
MCBL	Constant ε	0.5637	0.7365
	Elliptic ε	0.5586	0.7355
	% Difference	***0.90***	***0.13***

Figure 18 shows the mean axial velocity along vertical lines. The plots are shown at distances 2D (a,c) and 6D (b,d) downstream of the respective turbines. Note that turbine 2 is located 7D downstream of turbine 1. Comparisons are made again for the two ALM spreading methods and both NBL and MCBL flow conditions. Velocity profiles obtained from the precursor ABL simulation (NBL as well as MCBL) are also shown for reference to assess how well the wake deficit has recovered. It can be seen that the ALM spreading method has only a relatively small effect on the mean velocity profiles. Comparing the two ABL states, the wake recovery is higher for the MCBL than for the NBL. However, the velocity profiles in the near wake downstream of the two turbines are quite different. While 2D downstream of turbine 1 the effect of flow acceleration through the hub area is visible, it is minimized 2D downstream of turbine 2. This can be attributed to enhanced turbulent mixing in the wake of turbine 1 before it interacts with turbine 2. Furthermore, it can be seen that, at 6D downstream of both turbines, the velocity deficit is higher for the lower half of the rotor disk area than for the upper half when compared to the respective mean ABL velocity profiles. This can be attributed to kinetic-energy entrainment from above the rotor disk area that is responsible for an accelerated wake recovery within the upper half of the rotor disk that has not yet diffused into the lower portions of the shear layer. This difference in the two halves of the rotor disk area is alleviated to a great extent for the MCBL flow due to enhanced vertical mixing. The velocity deficit 6D downstream of turbine 1 gives an idea of the flow power available for turbine 2. It can be concluded that the gain in power for turbine 2 in the MCBL is primarily contributed to by the lower half of the rotor disk. If there were a third turbine at 13D (from reference), the recovery pattern would be similar to that for turbine 2. This is consistent with the observation in a real wind farm where turbine power typically levels at the third turbine within an array.

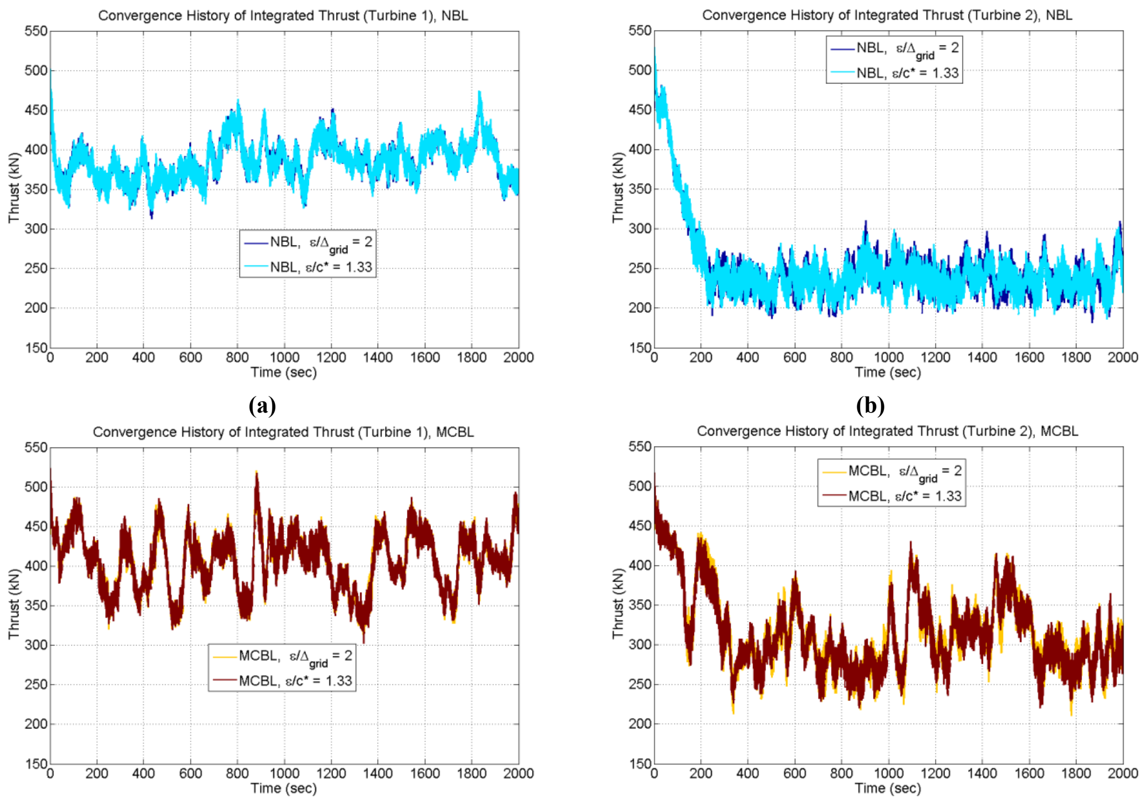

(a) (b) (c) (d)

Figure 17. Thrust histories for turbine-turbine interaction problem.
(a) Turbine 1 (NBL) (b) Turbine 2 (NBL) (c) Turbine 1 (MCBL) (d) Turbine 2 (MCBL)

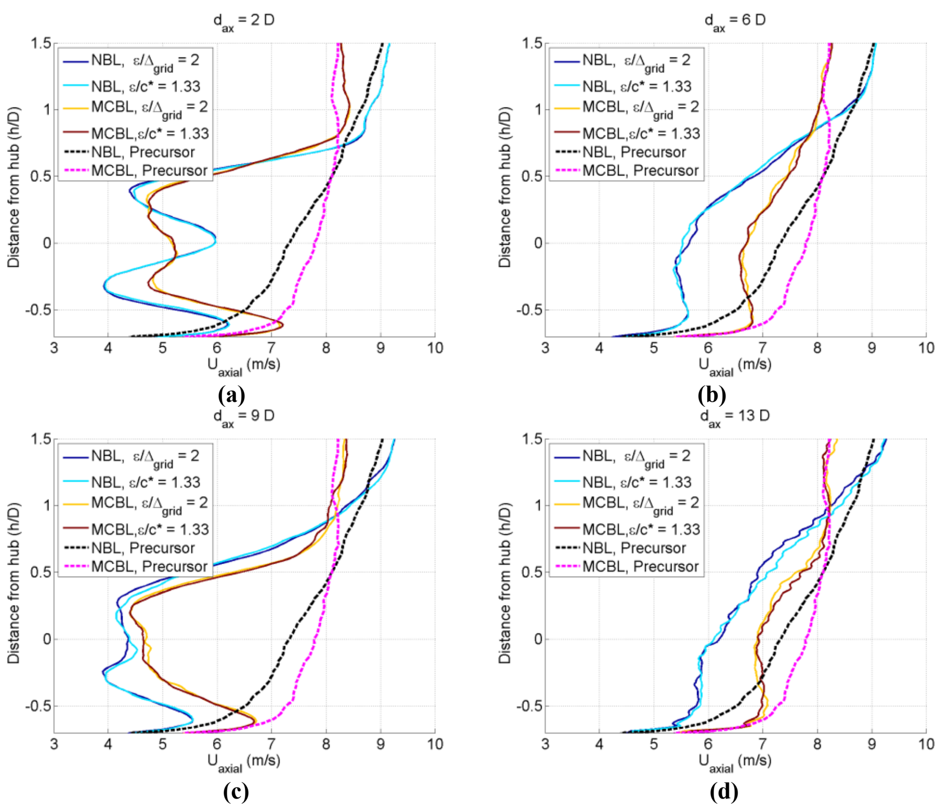

(a) (b) (c) (d)

Figure 18. Mean streamwise velocity distributions in the vertical direction.
(a) 2D downstream of Turbine 1 (b) 6D downstream of Turbine 1
(c) 2D downstream of Turbine 2 (d) 6D downstream of Turbine 2

Figure 19 shows the mean axial velocity along the horizontal lines at hub height. The observations are similar to those along vertical lines, except for those due to velocity shear. One important observation in contrast to those made along vertical lines is that the velocity profile shifts leftwards in the far wake for the MCBL flow. At 6D downstream of both turbines, the wake has meandered about 1D, i.e., the peak velocity deficit has drifted one rotor diameter from the hub axis. Since the velocity profile at 6D downstream of each turbine is representative of the power available for the next downstream turbine, the downstream turbine is expected to encounter higher unsteady loadings due to the observed wake meandering. Therefore, while the MCBL helps in recovering the velocity deficit and hence enhancing the power production by the downstream turbines, the unsteady loading due to up- and downdrafts in addition to wake meandering may be detrimental to the structural health of downstream turbines.

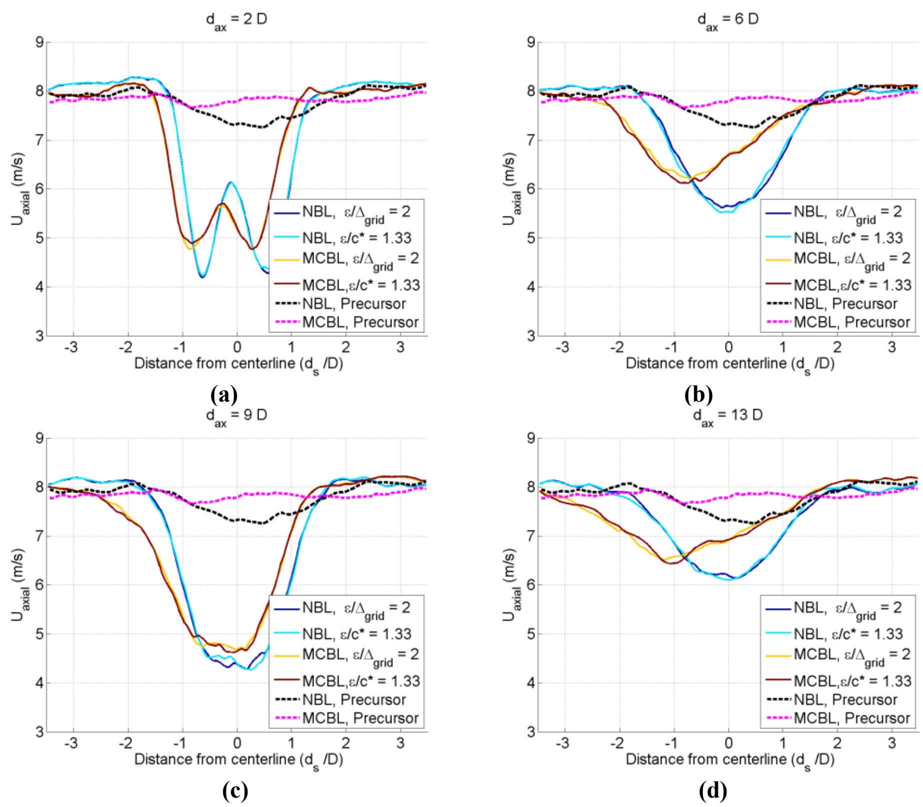

Figure 19. Mean streamwise velocity distributions in the spanwise direction at hub height.
(a) 2D downstream of Turbine 1 (b) 6D downstream of Turbine 1
(c) 2D downstream of Turbine 2 (d) 6D downstream of Turbine 2

We have thus far observed that the mean velocity profiles are affected by the ABL states and exhibit different behavior at different downstream locations. While the ALM spreading method had some noticeable effect on mean turbine power and its standard deviation, it has a smaller effect on the mean velocity profiles in the wakes of the turbines. However, it is expected that the difference in tip loads observed in Fig. 6 result in subtle differences in the tip vortices for the two ALM spreading methods. The tip vortices, though, do affect the turbulence in the wake. It is therefore important to investigate the turbulent kinetic energy (TKE) and Reynolds stresses. The convention for describing the Reynolds stresses is the following: The first direction is the axial one, the second direction (positive) is the rightward spanwise direction (when looking from a downstream location), and the third direction is the vertical direction.

Figures 20 and 21 show TKE distributions along vertical and horizontal lines, respectively. Similar to Figs. 18 and 19, the results are presented for 2D (a,c) and 6D (b,d) downstream of both the turbines, and comparisons are made between the two ABL states and both ALM spreading methods. As expected, the TKE is higher for the MCBL than for the NBL downstream of the first turbine in Fig. 20(a). It is interesting to note, though, that the TKE in the NBL grows at a higher rate in the turbine wakes than in the MCBL, see Fig. 20(b-d). The meandering of the wake is also evidenced by the shift of TKE concentration along the horizontal lines in Fig. 21. One additional interesting observation is that the TKE for the two ALM spreading methods differs mostly along the inner part of the rotor disk between $z/D = +/- 0.5$. While the ALM spreading method according to $\varepsilon/\Delta_{grid}$ shows slightly higher TKE inboard, a Gaussian spreading following the ε/c^* criterion exhibits slightly higher TKE injected by the tip vortices, see Fig. 20(a,c). It is hypothesized that this is related to the fact that Gaussian spreading following ε/c^* leads to tighter tip vortices than for the $\varepsilon/\Delta_{grid}$ method due to a smaller Gaussian radius ε at the blade tips.[14] The situation is reversed around the mid-blade location $z/D = +/- 0.25$, and, indeed, the TKE levels are higher for the $\varepsilon/\Delta_{grid}$ method than for the ε/c^* criterion. This indicates that body-force projection as used in today's ALMs generates local TKE somewhat anti-proportional to the Gaussian spreading radius ε. It also supports another hypothesis, i.e. that coarse grids may generate tip vortices with too large cores and consequent too low TKE. To date, there is, unfortunately, no data available that could be used for additional validation of various ALM methods and the TKE that is being generated by the actuator lines.

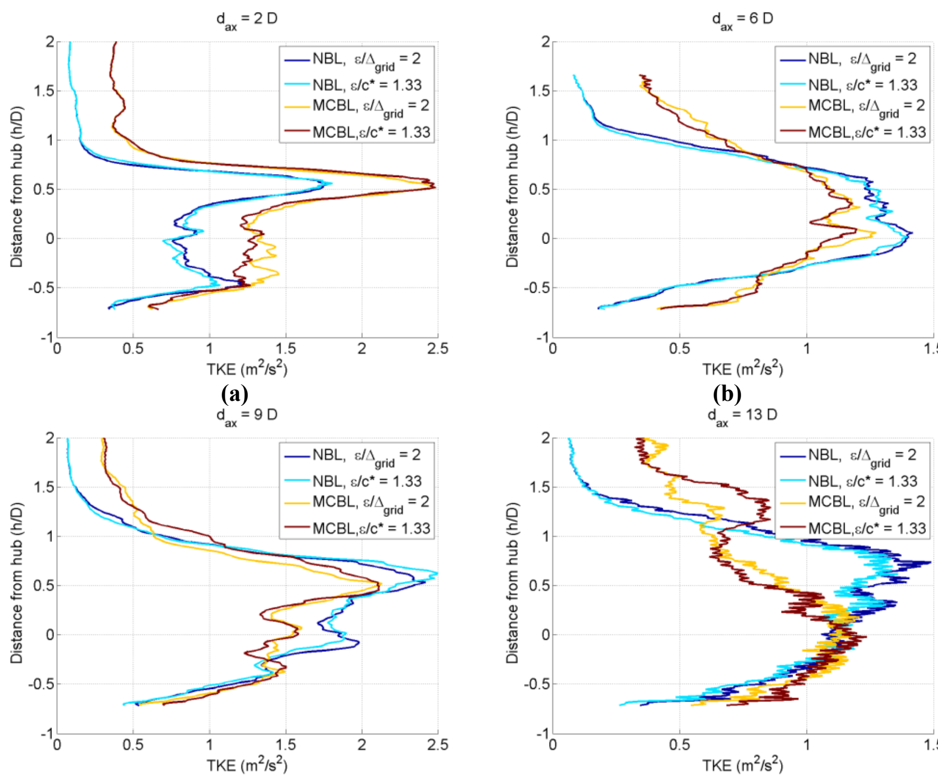

(a) (b) (c) (d)

Figure 20. TKE distribution in the vertical direction.
(a) 2D downstream of Turbine 1 (b) 6D downstream of Turbine 1
(c) 2D downstream of Turbine 2 (d) 6D downstream of Turbine 2

Figures 22 and 23 show R_{11} on vertical and horizontal lines, respectively. The Reynolds stress R_{11} is representative of the fluctuations in the power available in the wind. At 2D downstream, the MCBL shows higher correlation, while at subsequent downstream locations the correlation is higher for the NBL. This observation is in accordance with the sectional loads and histories of power and bending moment. As for TKE, R_{11} shows some difference between the two ALM spreading methods. Note that R11 (and all subsequent Reynolds stresses) were averaged between $t = 100$ s – 2,000 s. A lateral shift in the peak at 6D downstream of both turbines for the MCBL in Fig. 23 confirms once more wake meandering. Further insight into the wake meandering process can be gained by investigating the correlation of streamwise and spanwise velocities. Figure 24 shows R_{12} along horizontal lines at 2D and 6D downstream of the two turbines. The sign change of R_{12} about the wake centerline, and the increase of R_{12} with distance in the wake are associated with wake diffusion as a result of stronger mixing of the wake flow with the freestream wind above the rotor disk area. The lateral shift of the peaks at 6D for the MCBL is again attributed to wake meandering. Both ALM spreading methods show very similar distributions and trends. Finally, Fig. 25 shows R_{13} along vertical lines. Similar to Fig. 24, the wake diffusion in the vertical direction can be observed. The correlations become noisier at 13D. Small differences between the two ALM spreading methods are noted but they follow overall the same trends.

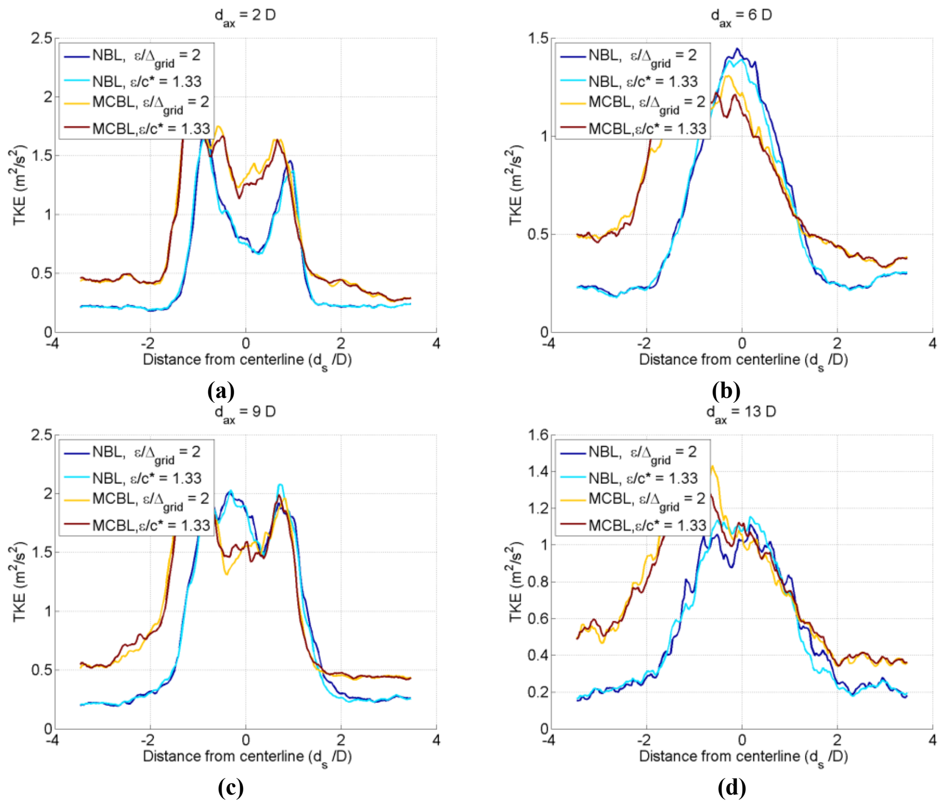

Figure 21. TKE distribution in the spanwise direction at hub height.
(a) 2D downstream of Turbine 1 (b) 6D downstream of Turbine 1
(c) 2D downstream of Turbine 2 (d) 6D downstream of Turbine 2

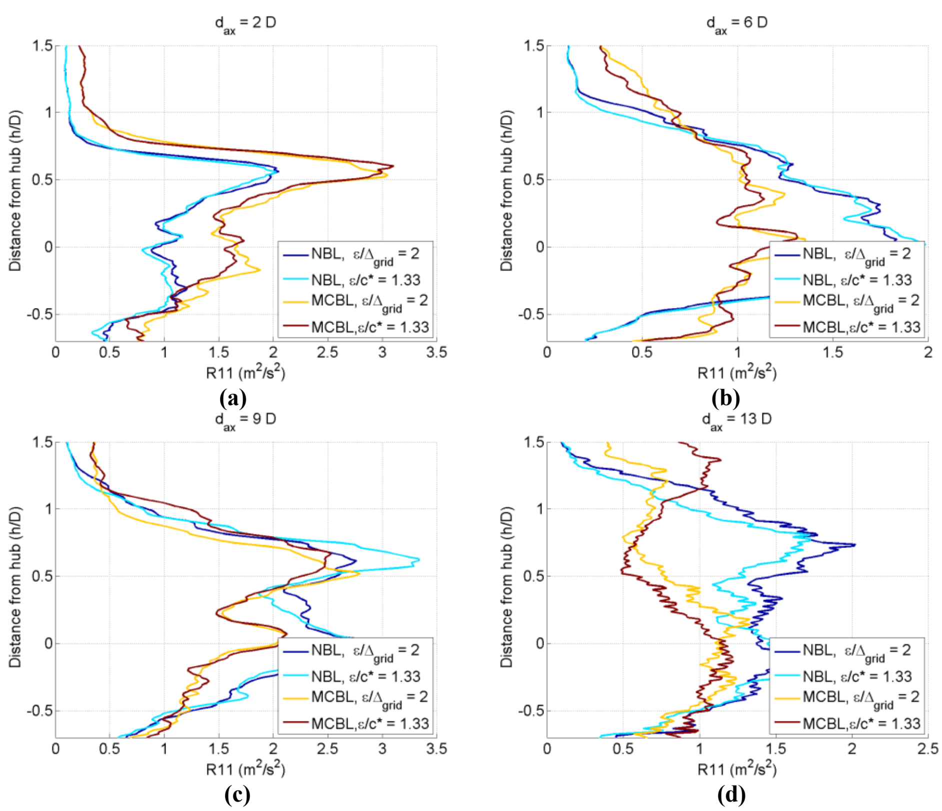

Figure 22. R11 distribution in the vertical direction.
(a) 2D downstream of Turbine 1 (b) 6D downstream of Turbine 1
(c) 2D downstream of Turbine 2 (d) 6D downstream of Turbine 2

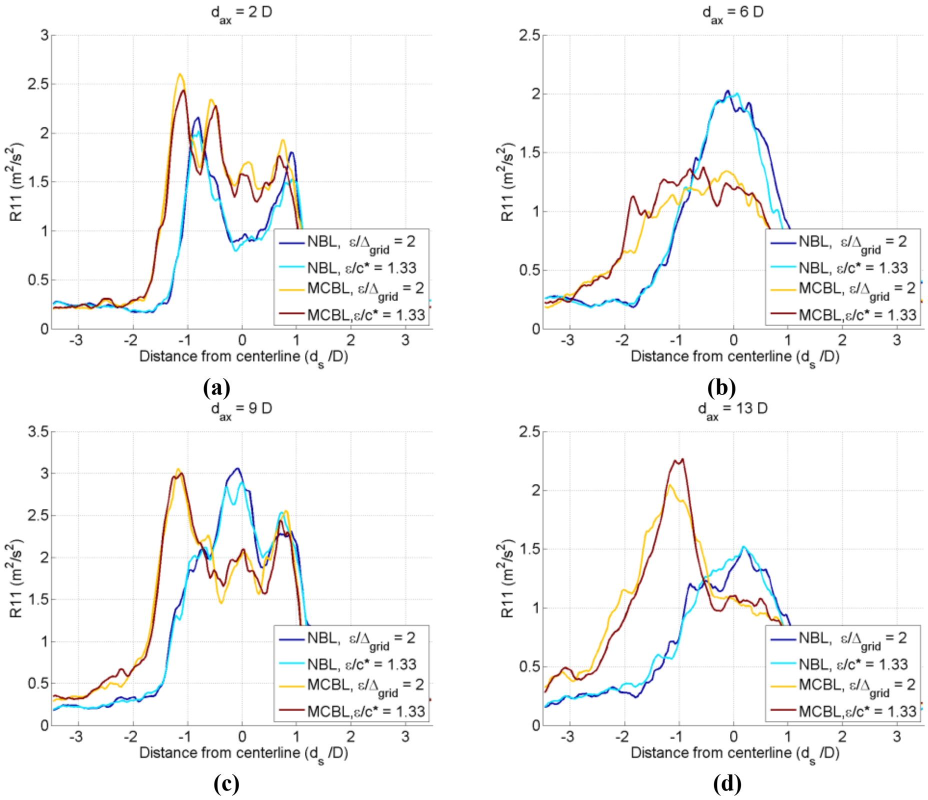

Figure 23. R11 distribution in the spanwise direction at hub height.
(a) 2D downstream of Turbine 1 (b) 6D downstream of Turbine 1
(c) 2D downstream of Turbine 2 (d) 6D downstream of Turbine 2

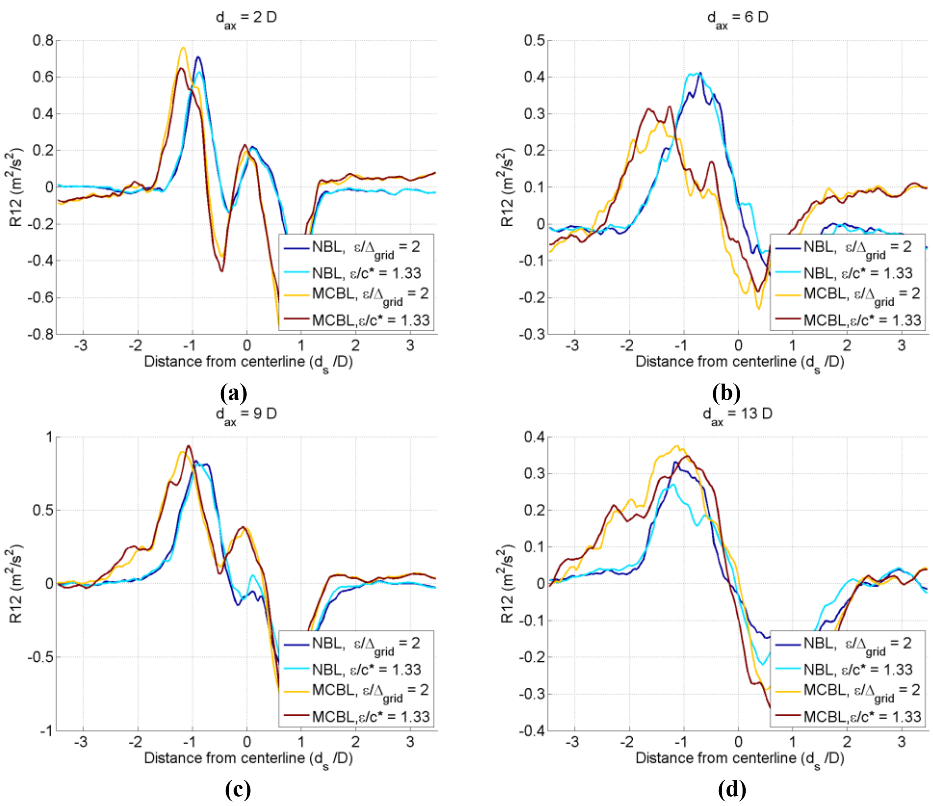

Figure 24. R12 distribution in the spanwise direction at hub height.
(a) 2D downstream of Turbine 1 (b) 6D downstream of Turbine 1
(c) 2D downstream of Turbine 2 (d) 6D downstream of Turbine 2

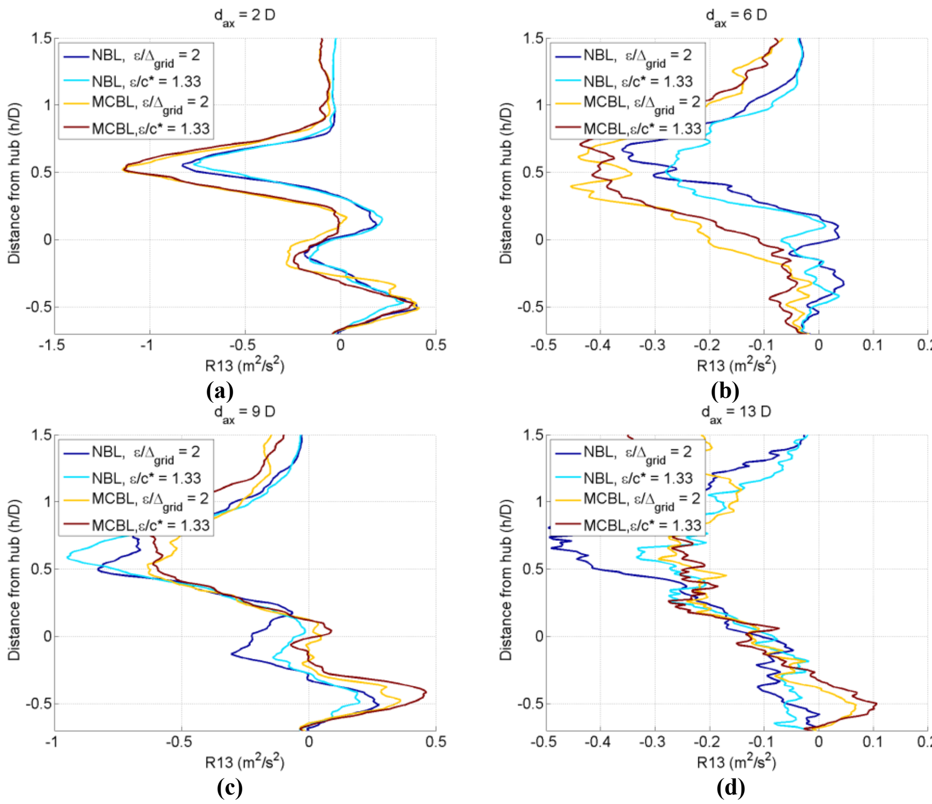

Figure 25. R13 distribution in the vertical direction.
(a) 2D downstream of Turbine 1 (b) 6D downstream of Turbine 1
(c) 2D downstream of Turbine 2 (d) 6D downstream of Turbine 2

IV. Conclusion

Actuator line modeling is becoming increasingly important as a Computational Fluid Dynamics tool that is both accurate and computationally efficient in modeling and predicting the performance of multiple wind turbine arrays and entire wind farms. While a lot of effort has been given towards predicting wake velocity deficits and turbulence statistics downstream of wind turbines and deep into large wind farms, not much attention has been given to predicting the spanwise blade loads of individual turbine blades and their local response to variable atmospheric inflow conditions. Recently, a variation of the original actuator-line method developed by Sørensen and Shen has been proposed by Jha et al. in which the Gaussian spreading radius ε follows an elliptic distribution along the blade span. It was found that the new ε/c^* criterion leads to improved prediction of local blade loads, when compared to measured data, and also to consistent results between various levels of grid refinement and turbine blade geometries compared to the original $\varepsilon/\Delta_{grid}$ criterion.

The objective of this paper was to assess how differences in both actuator line methods affect local as well as integrated turbine quantities such as the turbine power, thrust, and root-flap bending moment along with vertical and spanwise (horizontal) wake velocity deficits and selected Reynolds stresses at various locations in the wake. Two atmospheric stability states were considered, i.e. a neutral and a moderately-convective atmospheric boundary layer representative of an offshore environment. The simulations were limited to an array of two NREL 5-MW wind turbines separated by seven rotor diameters. It was found that a difference in mean turbine power of the order of 4 percent occurs as a result of the specific actuator-line method. This difference was mainly attributed to a difference in local blade loads outboard of the r/R = 0.85 spanwise blade station. As such, for the first turbine in an array, the discrepancy between particular actuator-line modeling approaches is of the same order than the variations associated with the atmospheric stability state itself. This is potentially important for estimating blade fatigue and associated O&M costs as well as array performance. These differences starting with the local blade angle of attack outboard of the r/R = 0.85 spanwise station are truncated into the respective turbine wakes and are observed in the wake deficits and turbulence statistics. This gives confidence that the underlying large-eddy simulation solver does not artificially (numerically) dissipate these differences. For future research, it would be very interesting to further analyze the data in order to study in greater detail the difference in the tip-vortex core size and its instability process between both actuator-line modeling approaches.

The true message, though, to the wind energy community is the following: An uncertainty of only one percent in the performance of a large wind farm, for example the Horns Rev wind farm in Denmark, can cost an operator more than one million dollars per year. While the present work pushes the physical and accuracy limits of state-of-the-art actuator-line modeling, there is a need for the wind energy community to define the new requirements for modeling accuracy of wind farm wake models. It is apparent that modeling accuracy is still not at a sufficient level, and the community of wind energy researchers is tasked with both finding innovations to the current modeling techniques but also to advance modeling fidelity on highly parallel computing systems.

This work was supported by the Department of Energy (DE-EE0005481) as part of the "Cyber Wind Facility" project at the Pennsylvania State University and in collaboration with NREL.

V. References

1. Rathmann, O., Frandsen, S. T., Barthelmie, R. J., "Wake Modelling for Intermediate and Large Wind Farms," *Proceedings of the European Wind Energy Conference and Exhibition*, Milan, Italy, 2007.
2. Jensen, L. E., "Array Efficiency at Horns Rev and the Effect of Atmospheric Stability," Dong Energy Presentation, 2007.
3. Cyber Wind Facility Program, The Pennsylvania State University, http://www.wind.psu.edu/cyberwind/default.asp
4. Lavely, A.W., Vijayakumar, G., Jayaraman, B., Craven, B., Paterson, E. G., Nandi, T.N., and Brasseur, J.G., "A Blade-Resolved Hybrid URANS-LES of the NREL 5 MW Wind Turbine Rotor within Large Eddy Simulation of the Atmospheric Boundary Layer," *submitted to AIAA Aerospace Sciences Meeting (ASME Wind Energy Symposium),* 2014
5. Sørensen, J. N., Shen, W. Z., "Numerical modeling of Wind Turbine Wakes," *ASME Journal of Fluids Engineering,* **124**, 393-399, 2002.
6. OpenFOAM—The Open Source CFD Toolbox, Version 2.0.x, OpenCFD Ltd, a part of the ESI Group, 2013, http://www.openfoam.com.
7. Churchfield, M. J., Lee, S., Michalakes, J., and Moriarty, Patrick J., "A Numerical Study of the Effects of Atmospheric and Wake Turbulence on Wind Turbine Dynamics," *Journal of Turbulence*, Vol. 13, No. 12, 2012.
8. Churchfield, M. J., Moriarty, P. J., Vijayakumar, G., Brasseur, J., "Wind Energy-Related Atmospheric Boundary-Layer Large-Eddy Simulation Using OpenFOAM," *NREL/CP-500-48905*, 2010.
9. Churchfield, Matthew J., Lee, S., Moriarty, Patrick J., Martínez, Luis A., Leonardi, S., Vijayakumar, G. and Brasseur, J. G., "A Large-Eddy Simulation of Wind-Plant Aerodynamics," *AIAA 2012-0537*, Nashville, TN.
10. Lee, S., Churchfield, Matthew J., Moriarty, Patrick J., Jonkman, J., and Michalakes, J." Atmospheric and Wake Turbulence Impacts on Wind Turbine Fatigue Loadings," *AIAA 2012-0540*, Nashville, TN.
11. Lee, S., Churchfield, Matthew J., Moriarty, Patrick J., Jonkman, J., and Michalakes, J." A Numerical Study of Atmospheric and Wake Turbulence Impacts on Wind Turbine Fatigue Loadings," *ASME Journal of Solar Energy Engineering,* Vol 35, No. 13, 2013
12. Martínez, Luis A., Leonardi, S., Churchfield, Matthew J., and Moriarty, Patrick J., "A Comparison of Actuator Disk and Actuator Line Wind Turbine Models and Best Practices for Their Use," *AIAA 2012-0900*, Nashville, TN.
13. Jha, P. K., Churchfield, M. J., Moriarty, P. J., and Schmitz, S., "Accuracy of State-of-the-Art Actuator-Line Modeling for Wind Turbine Wakes," *AIAA 2013-0608*, 2013. Fort Worth, TX
14. Jha, P. K., Churchfield, M. J., Moriarty, P. J., and Schmitz, S., " Guidelines for Actuator Line Modeling of Wind Turbines on Large-Eddy Simulation-type Grids," *ASME Journal of Solar Energy Engineering*, (in press)
15. Jonkman, J., Butterfield, S., Musial, W., and Scott, G., "Definition of a 5-MW Reference Wind Turbine for Offshore System Development," National Renewable Energy Laboratory, NREL Report TP-500-38060, Feb. 2009.